Radiological Physics and Technology (2019) 12:185–193
https://doi.org/10.1007/s12194-019-00513-x

Appropriate echo time selection for quantitative susceptibility mapping

Yuki Kanazawa[1] · Yuki Matsumoto[2] · Masafumi Harada[1] · Hiroaki Hayashi[3] · Tsuyoshi Matsuda[4] · Hideki Otsuka[1]

Received: 29 November 2018 / Revised: 6 April 2019 / Accepted: 8 April 2019 / Published online: 12 April 2019

Abstract
The purpose of our study was to clarify the dependence of quantitative susceptibility mapping (QSM) on echo time (TE). We constructed a phantom consisting of six tubes; three tubes were filled with different concentrations (0.5, 1.0, and 2.5 mM) of gadopentetate dimeglumine (Gd-DTPA), and three were filled with different concentrations (100, 200, and 350 mg/mL) of calcium hydroxyapatite. Real and imaginary images from multi-echo spoiled gradient-echo data (12 echoes) were acquired. We then used four datasets with three serial echoes. The QSM procedure consists of four steps: field map estimation, phase unwrapping, background removal, and dipole inversion. For each sample, we compared the measured mean susceptibility value with the theoretical susceptibility value and conducted a linear regression analysis. Accordingly, the relationship between the measured susceptibility and concentration of Gd-DTPA was shown to agree well with the theoretical values (TEs = 16.4, 20.8, and 25.2 ms; slope = 0.24, $R^2 = 1.00$). Furthermore, the relationship between the measured susceptibility and concentration of hydroxyapatite also showed good linearity (TEs = 16.4, 20.8, and 25.2 ms; slope = −0.00121, $R^2 = 1.00$). In conclusion, the optimization of the TE in QSM makes it possible to obtain more detailed information regarding the susceptibility of biomaterials.

Keywords Quantitative susceptibility mapping (QSM) · Echo time (TE) · Morphology-enabled dipole inversion (MEDI) · Paramagnetic · Diamagnetic

1 Introduction

Susceptibility is a very important physical factor in magnetic resonance imaging (MRI), indicating the characteristic value of a magnetic biomaterial in relation to magnetization. In the brain, there are many biomaterials with different magnetic susceptibilities: paramagnetic nonheme iron (ferritin), such as the red nucleus, 0.08 ppm; substantia nigra, 0.13 ppm; thalamus, 0.03 ppm; caudate nucleus, 0.06 ppm; putamen, 0.09 ppm; globus pallidus, 0.16 ppm: paramagnetic heme iron (deoxyhemoglobin, methemoglobin, and hemosiderin), such as vein, 0.45 ppm; gray matter, 0.02 ppm; and cerebrospinal fluid, 0 ppm [1]. Calcification, having diamagnetic biomaterial characteristics, has particularly less susceptibility (with a value of about − 11.3 ppm) compared to the other brain tissues [2]. These tissues and biomaterials may change with age in the subjects. Susceptibility changes in tissues are useful for detecting various diseases, such as those showing morphological characteristics and biological changes when using some images, e.g., T_2^*-weighted imaging, susceptibility-weighted imaging (SWI) [3], and quantitative susceptibility mapping (QSM) [4].

SWI is an imaging technique that presents the contrast between the susceptibility of biomaterials by multiplying a phase mask against the magnitude of the image [3]. This technique allows operators to obtain high-resolution images that are sensitive to magnetic susceptibility. In a clinical setting, SWI allows clearer visualization of microbleeding and

✉ Yuki Kanazawa
yk@tokushima-u.ac.jp

1 Institute of Biomedical Sciences, Tokushima University Graduate School, 3-18-15, Kuramoto-Cho, Tokushima, Tokushima 770-8503, Japan

2 Graduate School of Health Science, Tokushima University, 3-18-15, Kuramoto-Cho, Tokushima, Tokushima 770-8503, Japan

3 College of Medical, Pharmaceutical and Health Sciences, Kanazawa University, 5-11-80 Kodatsuno, Kanazawa, Ishikawa 920-0942, Japan

4 High-Field MRI Institute, Iwate Medical University, 19-1 Uchimaru, Morioka, Iwate 020-8505, Japan

smaller veins than T_2^*-weighted imaging. However, because SWI only emphasizes the phase-difference between tissues, it cannot assess the magnetic effect quantitatively, making it difficult to distinguish between diamagnetic and paramagnetic biomaterials [5].

QSM is a technique that can calculate the magnetic susceptibility of tissues based on the phase information of MRI [4]. In QSM, the local field is generated by convolving the susceptibility of surrounding materials with a dipole kernel. QSM reconstruction from MR phase data is performed as follows. First, the frequency offset is estimated in a voxel-by-voxel form from MR phase data. Phase unwrapping is then performed using a frequency map. The background phase information must be removed at this step. Finally, QSM enables the quantitative evaluation of diamagnetic and paramagnetic biomaterials using background-removed phase data. Several reports have described the usage of QSM in clinical applications, e.g., the visualization of iron deposits and calcification in the brain [6, 7] and diagnosis of Alzheimer's disease and Parkinson's disease [4].

QSM generally generates data from two types of images, real and imaginary images, with three-dimensional gradient-echo (3D-GRE) sequences acquired using either multiple or single echoes [8, 9]. One advantage of the single-echo technique is the ability to reduce the number of data. However, if there are variations such as eddy currents or B_1 inhomogeneity in the real and imaginary images, susceptibility estimation error can occur [10]. The multi-echo technique overcomes these susceptibility estimation errors using a fitting process [10]. Furthermore, since the susceptibility of each tissue is different, the T_2^* decay [or echo time (TE)] of each tissue must be considered; if the susceptibility is strong, then a short TE is selected, and if it is weak, then a long TE is selected [1, 4]. In addition, small TE increments may be used to achieve adequate signal-to-noise ratio (SNR) [4].

Most studies on QSM have focused on the methodology of the processing algorithms, and relatively few have discussed the method of data acquisition. Recently, some reports have focused on the relationship between TE and susceptibility in QSM data acquisition [11–13]. Fiber orientation-dependent white matter contrast in gradient-echo MRI was demonstrated with QSM of a two-pool model; water in the myelin sheath has a reduced T_2 relaxation time and spin density relative to its surroundings and also undergoes exchange [11]. Moreover, Sood et al. have reported that the selected of echo time affects the estimated susceptibility value in the human brain [13]. Therefore, it is quite likely that the TE setting depends on the accuracy of quantitative analysis using QSM, such as assessment of contrast activity in tissue and determination of biomaterial and tissue. We assumed that the estimated linearity of susceptibility value of QSM would depend on the acquired data at TE setting according to the material. The purpose of our study was to clarify the influence of TE on QSM.

2 Materials and methods

2.1 Phantom components

We created a phantom for this study. Figure 1 shows the schematics of the phantom. The phantom had a diameter and length each of 130 mm. Our phantom was constructed with six polypropylene tubes (inner diameter, 7.98 mm; outer diameter, 8.00 mm); three tubes were filled with different concentrations (0.5, 1.0, and 2.5 mM) of gadopentetate dimeglumine (Gd-DTPA; Magnevist, Bayer Pharma AG, Germany), and the three others were filled with different concentrations (100, 200, and 350 mg/mL) of calcium hydroxyapatite ($3Ca_3(PO_4)_2{\cdot}Ca(OH)_2$; Kishida Chemical Co., Ltd., Osaka, Japan). A theoretical value of Gd-DTPA was determined as 326 ppm L/mol at 293 K [14]. The susceptibility values of each Gd-DTPA solution at room temperature (24 °C) were 0.16, 0.32, and 0.8 ppm, respectively.

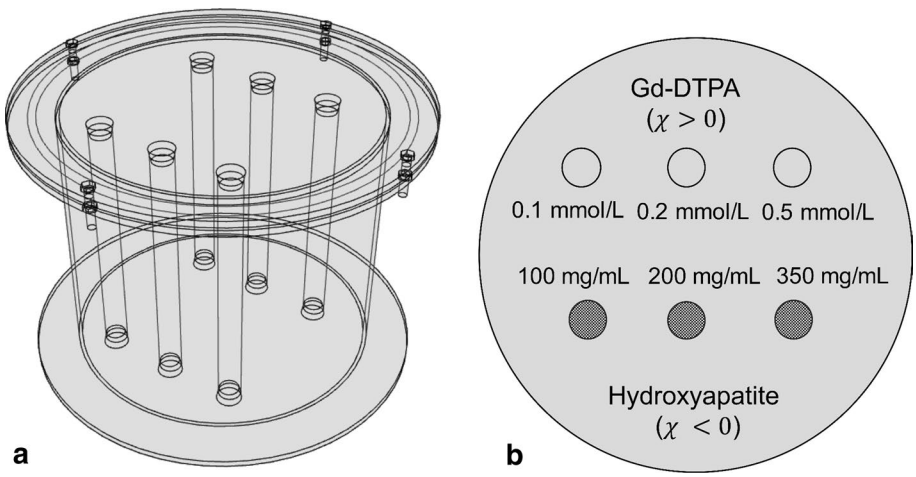

Fig. 1 A schematic overview of the QSM phantom that was used in this study. We created a cylindrical phantom consisting of six tubes. **a** The six tubes were sealed with silicon plugs. The cylindrical phantom was sealed with an acrylic lid. **b** The phantom was made with three different concentrations of Gd-DTPA and hydroxyapatite

Hydroxyapatite was uniformly suspended in 2% agarose gel to avoid sedimentation and the concentrations of 100, 200, and 350 mg/mL were adjusted in accordance with Henkelman et al.'s report [15]. These tubes were immersed in a cylindrical phantom filled with 2% agarose gel and sealed with caps to avoid air entering the cylindrical phantom and each tube.

2.2 Imaging parameters for QSM

On a 3.0-T MRI system (Discovery MR750; GE Healthcare, Waukesha, WI, USA), a phantom study was performed using 3D spoiled gradient-echo (SPGR) sequence with multiple TEs. The phantom was placed in the center of a quadrature head coil (as a receiver). The imaging parameters for QSM were TE, 12 echoes, from 3.1 to 51.7 ms [echo spacing = 4.4 ms: TE dataset was # 1, 2, 3 (TEs = 3.1, 7.5, and 11.9 ms); #4, 5, 6 (TEs = 16.4, 20.8, and 25.2 ms); #7, 8, 9 (TEs = 29.6, 34.0, and 38.4 ms); #10, 11, 12 (TEs = 42.8, 47.3, and 51.7 ms)]; repetition time (TR), 55.5 ms; matrix size, 256 × 256; slab thickness, 24 mm; spatial resolution, 1.0 × 1.0 × 1.0 mm; and pixel bandwidth, 244.1 Hz. The phantom was set perpendicular to the main field.

2.3 QSM and T_2^* mapping procedures

For QSM, we acquired real and imaginary images from MRI. We then used four datasets with three serial echoes. Figure 2 describes the procedure of QSM reconstruction. The QSM procedure consists of four steps: field map estimation, phase unwrapping, background removal, and dipole inversion. When estimating a field map from real and imaginary images, either a multi-echo or single-echo technique may be used [10]. The multi-echo technique was used in this study. Spatial phase unwrapping was performed using a Laplacian operator [16]. The background was removed using the Laplacian boundary value method [17]. Following background removal, dipole inversion was performed using morphology-enabled dipole inversion (MEDI) to reconstruct the susceptibility [18, 19]. A regularization parameter, lambda of MEDI, was then set at 1000. To reconstruct susceptibility, magnitude images from real and imaginary images were combined using all echoes via the sum-of-squares method to obtain a sufficient signal-to-noise ratio (SNR).

Moreover, to calculate the SNR of the signal phase, T_2^* mapping was generated. Nonlinear curve fitting was then performed on each voxel using the Levenberg–Marquardt algorithm, which can be represented as follows:

$$I(\mathrm{TE}) = M_0 \mathrm{e}^{-\frac{\mathrm{TE}}{T_2^*}}, \tag{1}$$

$$\therefore \left[M_0, T_2^*\right] = \arg\min_{M_0, T_2^*} \left(\sum_{i=1}^{N_{\mathrm{TE}}} \left(\left(i(\mathrm{TE})_i - I(\mathrm{TE})_i(\alpha_i) \right)^2 \right) \right), \tag{2}$$

where I(TE) is the MR signal of each TE, M_0 is the equilibrium magnetization, and i(TE) is the theoretical signal value. Using varying α values, a nonlinear curve fitting procedure can then yield an estimation of parameters for M_0 and T_2^* according to the relationship between MR signal and TE.

All post-processing was carried out using MATLAB R2016a (MathWorks, Inc., Natick, MA, USA). QSM algorithms were customized programs based on code distributed online (http://weill.cornell.edu/mri/pages/qsm.html). We performed our analyses on a Mac Pro workstation (six cores, Xeon 3.3 GHz with 32 GB RAM).

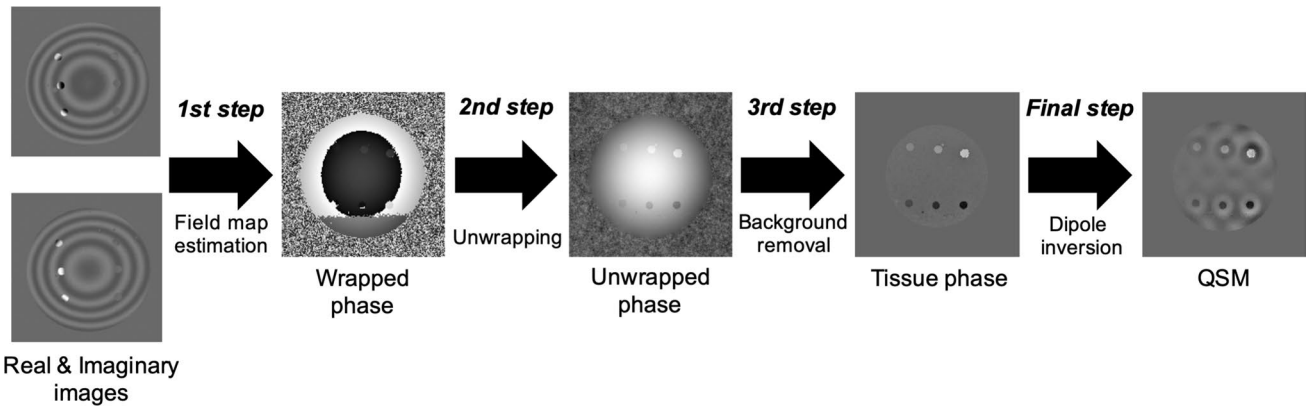

Fig. 2 Schematic illustration of the QSM reconstructive procedure. The steps were as follows: field map estimation, phase unwrapping, background removal, and dipole inversion

2.4 Region of interest analysis

To measure the susceptibility value from QSM, we manually set the region of interest (ROI) to the inside of each tube (the circular ROIs were set at 30 pixels) using the same location for each TE dataset. We then measured the susceptibility values in the ROI from the middle slice of the QSM volume data; we set the ROI to the backward or forward three images for center of the middle section and measured the mean value for the three slices. For Gd-DTPA, we compared the measured mean susceptibility value with the theoretical susceptibility value and performed a linear regression analysis. For hydroxyapatite, we performed a linear regression analysis between the different hydroxyapatite concentrations. To evaluate the error in susceptibility for each dataset, we adopted a circular standard deviation ($SD_{circular}$) derived from the circular statistics of phase data in the ROI. $SD_{circular}$ can be derived from the mean resultant length that is the length of the average vectors calculated from all phase angles in the ROI. Here, the mean resultant length $\bar{R}$ is described as follows:

$$\bar{R} = \frac{1}{n}\sum_{j=1}^{n}\cos(\theta_j - \bar{\theta}) \in [0, 1], \tag{3}$$

where θ_j is the phase data of each pixel in the ROI, and $\bar{\theta}$ is the mean phase data direction in the ROI. $SD_{circular}$ is described as the following relationship:

$$SD_{circular} = \sqrt{-2\log\bar{R}} \in [0, \infty]. \tag{4}$$

Using the $SD_{circular}$ enables us to perform an evaluation because the phase shift increases in a voxel without echo-convergence.

The ROI analyses were performed using in-house software made using MATLAB. Statistical analyses, such as the evaluation of linearity, were performed using the R software package (version 3.2.5; The R Foundation for Statistical Computing, Vienna, Austria).

3 Results

Table 1 shows the susceptibility values for Gd-DTPA and hydroxyapatite in each sample ROI on different TE dataset QSM. Moreover, the bottom row shows the mean T_2^* values for Gd-DTPA and hydroxyapatite in the ROI of each sample.

Table 2 shows the $SD_{circular}$ values of each sample in the field map estimation. Each $SD_{circular}$ value from different TE dataset is also shown.

Figure 3 shows the QSM derived from MEDI for each TE dataset. From left to right, the TE datasets are shown in order of larger TE. Figure 3a shows the dataset for the lowest TEs (TEs = 3.1, 7.5, and 11.9 ms), and Fig. 3d shows the dataset for the highest TEs (TEs = 42.8, 47.3, and 51.7 ms). The susceptibility values ranged from −0.5 to 1.5 ppm. For the Gd-DTPA samples (upper three samples in the phantom images) in each dataset, a high signal corresponding with the concentration of Gd-DTPA was observed. For the hydroxyapatite samples (lower three samples in the phantom images) in each dataset, a signal lower than that for

Table 2 $SD_{circular}$ values of each sample for field map estimation of imaging procedures

Concentrations of each material	$SD_{circular}$ values			
	1, 2, 3	4, 5, 6	7, 8, 9	10, 11, 12
Gd-DTPA				
0.5 mM	0.083	0.082	0.084	0.086
1.0 mM	0.061	0.059	0.060	0.061
2.5 mM	0.078	0.078	0.080	0.081
Hydroxyapatite				
100 mg/mL	0.091	0.099	0.117	0.129
200 mg/mL	0.103	0.074	0.664	1.256
350 mg/mL	0.104	0.159	0.879	1.764

Table 1 Magnetic susceptibility values for Gd-DTPA and hydroxyapatite in each sample

Echo numbers	Susceptibility (ppm)					
	Gd-DTPA			Hydroxyapatite		
	0.5 (mM)	1 (mM)	2.5 (mM)	100 (mg/mL)	250 (mg/mL)	300 (mg/mL)
1, 2, 3	0.24 ± 0.01	0.30 ± 0.02	0.78 ± 0.03	−0.02 ± 0.01	−0.01 ± 0.04	−0.15 ± 0.04
4, 5, 6	0.25 ± 0.01	0.38 ± 0.02	0.72 ± 0.05	−0.16 ± 0.02	−0.23 ± 0.07	−0.50 ± 0.07
7, 8, 9	0.26 ± 0.01	0.06 ± 0.05	0.79 ± 0.03	0.03 ± 0.03	0.14 ± 0.06	0.10 ± 0.04
10, 11, 12	0.24 ± 0.01	0.28 ± 0.04	0.47 ± 0.07	−0.16 ± 0.03	−0.01 ± 0.03	0.05 ± 0.07
1–12	0.02 ± 0.01	0.36 ± 0.04	0.73 ± 0.06	−0.07 ± 0.01	−0.05 ± 0.03	−0.17 ± 0.25
Theoretical value	0.16	0.32	0.8	–	–	–
T_2^* values (ms)	369.1	199.6	86.9	24.6	14.2	11.0

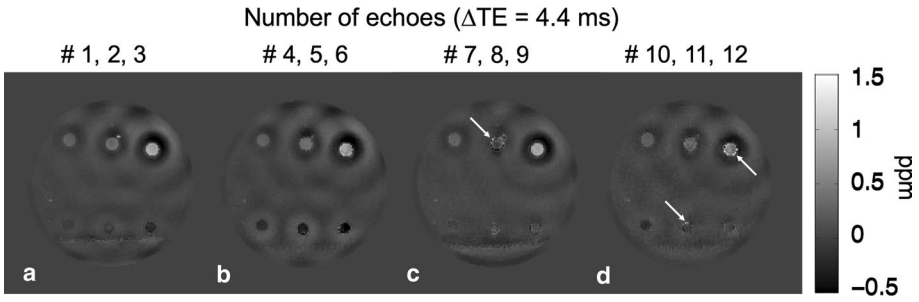

Fig. 3 Reconstructions from the QSM of each TE dataset. **a** Echo numbers 1, 2, 3 (TEs = 3.1, 7.5, and 11.9 ms); **b** echo numbers 4, 5, 6 (TEs = 16.4, 20.8, and 25.2 ms); **c** echo numbers 7, 8, 9 (TEs = 29.6, 34.0, and 38.4 ms); **d** echo numbers 10, 11, 12 (TEs = 42.8, 47.3, and 51.7 ms). The white arrows indicate the reconstruction errors

Gd-DTPA was observed. In the agar area around the Gd-DTPA and hydroxyapatite samples, low- and high-signal areas, respectively, were observed.

Figure 4 shows the relationship between the measured susceptibility value and concentration of Gd-DTPA or hydroxyapatite in each TE dataset. The relationship between the measured susceptibility and concentration of Gd-DTPA was shown to agree well with the theoretical value (Fig. 4b; slope = 0.24, $R^2 = 1.00$). Furthermore, the relationship between the measured susceptibility and concentration of hydroxyapatite also showed good linearity (Fig. 4f; slope = − 0.00121, $R^2 = 1.00$).

Figure 5 shows the QSM and plots of measured susceptibility value derived from the 1–12 TE dataset. The relationship between the measured susceptibility and concentration of Gd-DTPA was shown to agree well with the theoretical value (slope = 0.25, $R^2 = 1.00$). However, the relationship between the measured susceptibility and concentration of hydroxyapatite showed poor linearity (slope = − 0.00039, $R^2 = 0.75$).

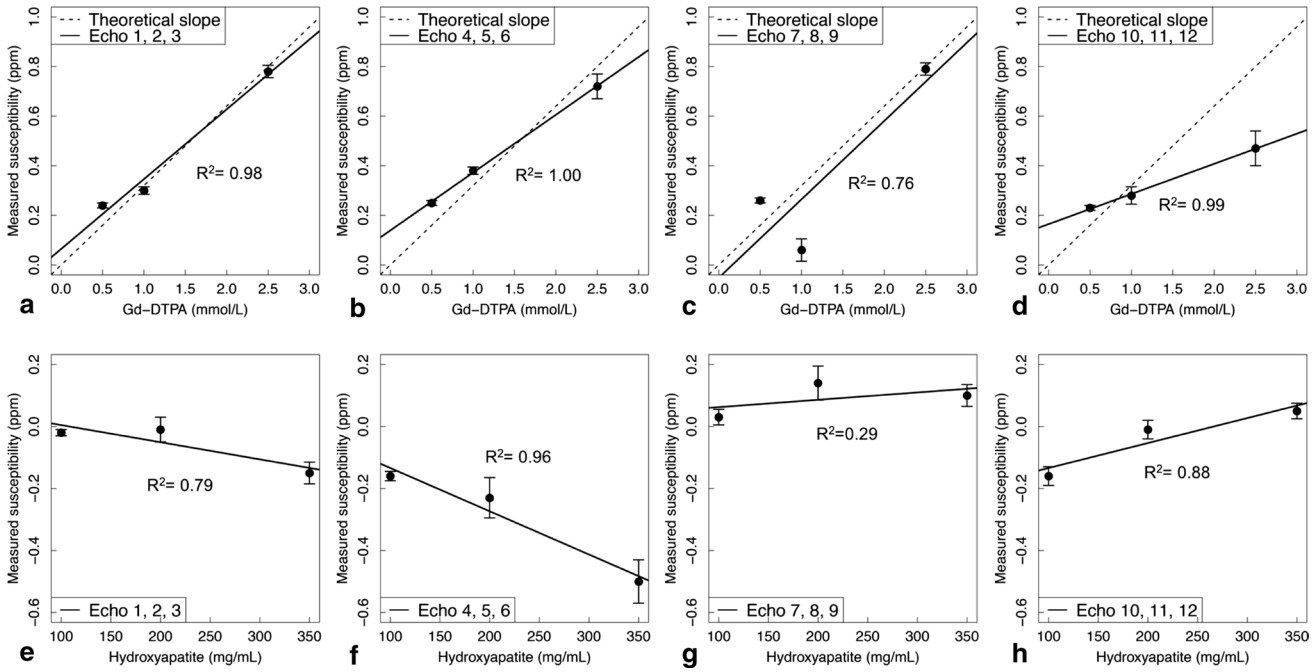

Fig. 4 The relationship between each construction of Gd-DTPA or hydroxyapatite and the measured susceptibility value. The top row (**a**–**d**) indicates the measured susceptibility values of each concentration of Gd-DTPA; the bottom row (**e**–**h**) indicates the measured susceptibility values of each concentration of hydroxyapatite. From left to right on each row, the TE for the dataset increases. The error bars show the standard deviation

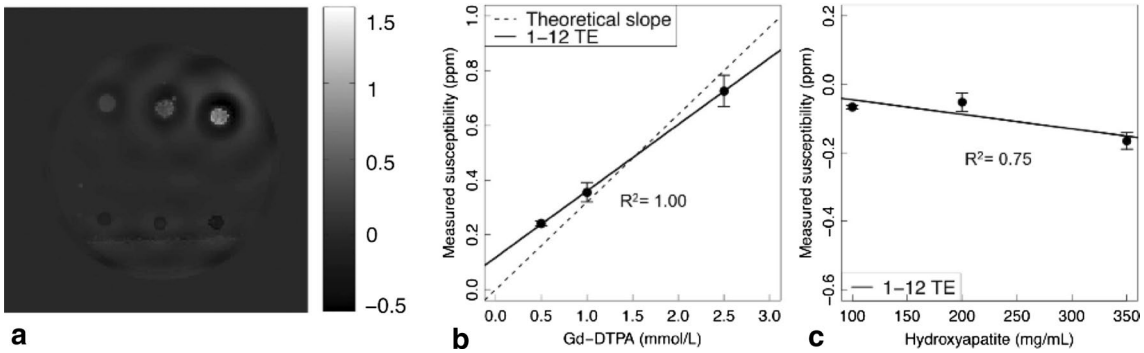

Fig. 5 QSM results derived from the total TE dataset. **a** A reconstructed image from the total TE dataset. **b** The relationship between measured susceptibility and each concentration of Gd-DTPA. **c** The relationship between measured susceptibility and each concentration of hydroxyapatite

4 Discussion

In this study, to clarify the influence of TE on a magnetic biomaterial, we evaluated the relationship between quantitative magnetic susceptibility and TE using QSM. Using a cylindrical phantom, which is used for paramagnetic and diamagnetic samples, QSM images were acquired for several TE datasets. We measured the susceptibility of each sample using QSM. The short TE datasets (#4, 5, 6) showed good linear relationships between susceptibility with concentrations of Gd-DTPA and hydroxyapatite (see Fig. 4). In contrast, in the long-TE datasets (#10, 11, 12), no significant correlation was noted between the measured susceptibility value and Gd-DTPA or hydroxyapatite concentration. These findings suggest that the difference in the QSM results may have been due to the influence of the TE dataset.

A previous study showed that SWI using a multi-echo GRE sequence was more useful in reducing the noise contribution than single-echo GRE [20]. In addition, Wu et al. clearly indicated that a frequency shift image requires an appropriate TE to obtain a high SNR and contrasted image [8]. While there have been some reports on the relationship between quantitative assessment and data acquisition methods, such as single-echo [21] and multi-echo [22], few reports have explored the relationship between data acquisition and susceptibility derived from the data acquisition for QSM. In our phantom study, e.g., in the short TE dataset, the quantitative evaluation of susceptibility indicated good assessments regarding the linearity of Gd-DTPA and hydroxyapatite concentrations (Fig. 4a, b, e, f). However, the accuracy of the linearity between each material concentration and susceptibility was relatively poor in the long-TE dataset (Fig. 4c, d, g, h). Let us discuss the MR signal phase in full detail. The MR signal can be described using the following approximate model [23]:

$$s(r, \mathrm{TE}) \approx \bar{m}\Delta V \mathrm{e}^{-\frac{\mathrm{TE}}{T_2^*}} \mathrm{e}^{-i\overline{b(r)}\gamma \mathrm{TE}}, \tag{5}$$

where $\bar{m}$ is the mean magnetization, V is the voxel volume, $\overline{b(r)}$ is the mean magnetic field, and γ is the gyromagnetic ratio. When using materials with weak susceptibility, a short TE, and few voxels, the phase signals can be used to measure the magnetic field generated by susceptibility [23]. However, when using materials with strong susceptibility and a long-TE setting, the approximation model in Eq. (1) cannot be adapted since the phase term $\mathrm{e}^{-i\overline{b(r)}\gamma \mathrm{TE}}$ becomes nonlinear in the TE [24]. The loss of phase information from the first echo acquired may cause short T_2^* signal components to be lost and significantly affect the measured frequency and QSM profiles [12]. Moreover, Sood et al. reported that the echo time dependence in various brain regions behaved as a function of the mapped value of susceptibility [13]; the susceptibility effect of micro-structures between the myelin and nerve fiber must be considered. It is, therefore, necessary to use an appropriate TE dataset.

In this study, we evaluated the calculation error of the concentration of each material and a different TE dataset at the field map estimation using circular statistical analysis (Table 2). $\mathrm{SD}_{\mathrm{circular}}$ values in the concentration of the hydroxyapatite sample indicated a higher variation than that in the concentration of the Gd-DTPA sample. Although the $\mathrm{SD}_{\mathrm{circular}}$ values were almost equal between the TE datasets in the Gd-DTPA sample, they varied depending on the TE dataset in the hydroxyapatite sample. In contrast, the SNR of the image phase, SNR_θ, at a single echo was calculated as follows [8]:

$$\mathrm{SNR}_\theta = \frac{2\pi f t M_0 \mathrm{e}^{-\frac{t}{T_2^*}}}{\sigma}, \tag{6}$$

where f is the offset frequency, t is the TE, $M_0\mathrm{e}^{-\frac{t}{T_2^*}}$ is the signal magnitude at TE, and σ is standard deviation derived from the white noise in the image. Equation (6) is then modified when the SNR_θ is derived from a multi-echo dataset. The SNR_θ of each dataset is calculated as follows [8]:

$$\mathrm{SNR}_\theta = \frac{2\pi f}{\sqrt{\sum_{n=1}^{N} \frac{1}{(M_m t_n)^2}\sigma}}, \tag{7}$$

where t_n is the nth TE, M_m is the signal magnitude $M_0 e^{-\frac{t}{T_2^*}}$ at t_n. The SNR_θ depends on the T_2^* for each material; the maximum SNR_θ will be obtained when the echo time is equal to T_2^* [8]. Figure 6 shows the SNR_θ for each TE dataset of the Gd-DTPA and hydroxyapatite samples. In the present study, the Gd-DTPA samples had relatively long T_2^* values; this SNR_θ did not reach the maximum value when the TE dataset was set to 10–12 echoes (see Table 1 at T_2^* value). In contrast, the hydroxyapatite samples had relatively short T_2^* values, and the maximum SNR_θ was reached at 3–6 echoes (see T_2^* value in Table 1). Indeed, the relationship between susceptibility and the hydroxyapatite concentration showed good linearity for the 4–6 echo dataset (Fig. 4f). The SNR_θ was in good agreement with the theoretical values, in which the maximum value was reached when T_2^* was equal to TE (Fig. 6). However, the linearity of the susceptibility of Gd-DTPA was good at 4–6 echoes even without the maximum SNR_θ (Fig. 4b). It is quite likely that the $\mathrm{SD}_{\mathrm{circular}}$ values in the field map estimation influenced the results of the reconstruction of susceptibility in the present study. Therefore, we believe it is possibly dependent on white noise (although our study did not measure data by serial imaging). Although the SNR_θ of Gd-DTPA increased with a long-TE dataset, some artifacts were observed in the samples (Fig. 4); artifacts may cause a measurement error. The results clearly show that the susceptibility of materials with a long T_2^* (such as Gd-DTPA) can be meaningfully determined, not by SNR_θ but by the initial phase signal derived from each TE dataset.

Each material used in the present study has individual magnetic susceptibility characteristics. Gd-DTPA has a molar susceptibility of 326 ppm L/mol at 293 K [14]; this value is generally acceptable. However, the susceptibility of hydroxyapatite was not treated as a known quantity since the hydroxyapatite was uniformly suspended in 2% agarose gel in this study. For this reason, hydroxyapatite samples of different concentrations were made based on the T_2 values referenced from a previous study [15]. We, therefore, feel there is considerable validity in this phantom component.

Some reports have described the usefulness of the MEDI algorithm for QSM [18, 19]. Liu et al. indicated that MEDI accurately provided the susceptibility of contrast agent in a phantom study (slope = 0.97; R = 1.00) [18]. In addition, Chen et al. found that MEDI was useful for identifying calcifications (sensitivity, 80.5%) and hemorrhages (sensitivity, 89.5%) in a total of 151 lesions (62 hemorrhages, 89 calcifications) of the brain [6]. Therefore, this methodology was also useful to us in the present study.

Optimizing the imaging parameters is important for accurately calculating the susceptibility. In this study, the number of echoes was set at 12 echoes, because several materials with various susceptibilities were being imaged, i.e., a wide susceptibility range. This number of echoes is generally used. In addition, when performing the field map estimation, the noise variance can be reduced by setting a low echo spacing time [10]. Thus, the echo spacing time was set at 4.4 ms in this study. In addition, the pixel bandwidth was set at 244 Hz to avoid susceptibility artifacts while maintaining a high SNR. Considering errors in the field map estimation,

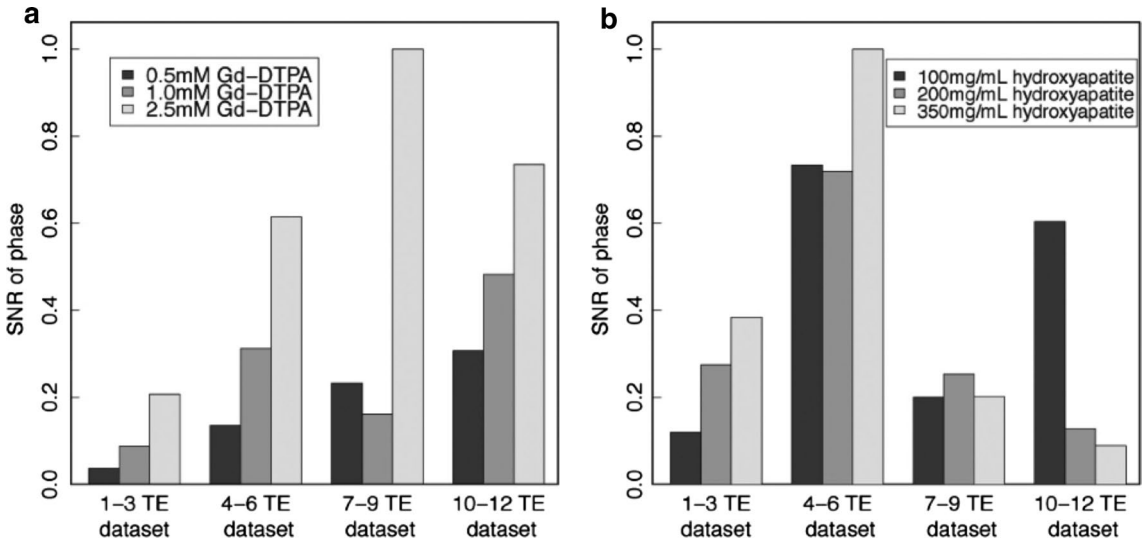

Fig. 6 SNR of phase at each TE dataset of Gd-DTPA (**a**) and hydroxyapatite (**b**) samples. The date were normalized by the maximum SNR value of Gd-DTPA and hydroxyapatite

the QD head coil was used as the receiver coil to simplify phase validations. It might be appropriate to apply imaging parameters for the evaluation of susceptibility in this study.

There were several limitations to our study. First, we used sample tubes in our phantom component. The MR signal did not occur from the wall of the sample tubes; as such, mobility protons and non-susceptibility distributions did not exist. If the phase value in the field of view (FOV) is derived from the susceptibility distributions, calculation of the susceptibility is completely possible [9]. However, although we used sample tubes with 0.02 mm wall thickness in this study, errors still occurred in QSM, as indicated by the white arrows in Fig. 3d. It might be necessary to use a thinner wall thickness in subsequent studies. Second, the QD head coil was chosen as the receiver coil to simplify phase validation. However, a multiple-phased array coil is generally used in clinical studies [25]. Evaluations using a multiple-phased array coil may be necessary before these findings can be applied in a clinical setting. Third, we did not evaluate the measured values of QSM using a reference signal in this study. Because all measurements are performed with phase information, evaluation with the absolute value of QSM includes digitization error in the phase image for QSM algorithm [18]. Normalized signals with reference may lead to a more accurate evaluation. Fourth, we did not calculate the theoretical susceptibility of hydroxyapatite, as stated above. Further, it must be shown in other studies of hydroxyapatite susceptibility. Finally, we did not consider other QSM reconstruction algorithms, such as the *k*-space approach [e.g., truncated *k*-space division (TKD)] [26] or Bayesian approach [e.g., total variation using split Bregman (TVSB)] [27]. Future studies should evaluate our phantom setup using these other QSM algorithms.

5 Conclusion

We evaluated the relationship between quantitative magnetic susceptibility and TE for QSM using a phantom composed of paramagnetic and diamagnetic samples. The TE dataset for QSM showed a good linear relationship with 16.4–25.2-ms TE at Gd-DTPA concentration ranging from 0.5 to 2.5 mM and hydroxyapatite concentration ranging from 100 to 350 mg/mL. It was noted from the results that the TE settings for the imaging dataset affected the accuracy of the estimated susceptibility value of QSM. Therefore, it seems reasonable to conclude that it is necessary to set the TE according to the material and/or tissue target.

Compliance with ethical standards

Conflict of interest The authors declare that they have no conflicts of interest.

Ethical approval This article does not contain any studies with human participants or animals performed by any of the authors.

References

1. Buch S, Liu S, Ye Y, Cheng YC, Neelavalli J, Haacke EM. Susceptibility mapping of air, bone, and calcium in the head. Magn Reson Med. 2015;73(6):2185–94.
2. Hopkins JA, Wehrli FW. Magnetic susceptibility measurement of insoluble solids by NMR: magnetic susceptibility of bone. Magn Reson Med. 1997;37(4):494–500.
3. Haacke EM, Xu Y, Cheng YC, Reichenbach JR. Susceptibility weighted imaging (SWI). Magn Reson Med. 2004;52(3):612–8.
4. Wang Y, Liu T. Quantitative susceptibility mapping (QSM): decoding MRI data for a tissue magnetic biomarker. Magn Reson Med. 2015;73(1):82–101.
5. Wu Z, Mittal S, Kish K, Yu Y, Hu J, Haacke EM. Identification of calcification with MRI using susceptibility-weighted imaging: a case study. J Magn Reson Imaging. 2009;29(1):177–82.
6. Chen W, Zhu W, Kovanlikaya I, Kovanlikaya A, Liu T, Wang S, et al. Intracranial calcifications and hemorrhages: characterization with quantitative susceptibility mapping. Radiology. 2014;270(2):496–505.
7. Schweser F, Deistung A, Lehr BW, Reichenbach JR. Differentiation between diamagnetic and paramagnetic cerebral lesions based on magnetic susceptibility mapping. Med Phys. 2010;37(10):5165–78.
8. Wu B, Li W, Avram AV, Gho SM, Liu C. Fast and tissue-optimized mapping of magnetic susceptibility and T2* with multi-echo and multi-shot spirals. Neuroimage. 2012;59(1):297–305.
9. Hsieh CY, Cheng YC, Neelavalli J, Haacke EM, Stafford RJ. An improved method for susceptibility and radius quantification of cylindrical objects from MRI. Magn Reson Imaging. 2015;33(4):420–36.
10. Kressler B, de Rochefort L, Liu T, Spincemaille P, Jiang Q, Wang Y. Nonlinear regularization for per voxel estimation of magnetic susceptibility distributions from MRI field maps. IEEE Trans Med Imaging. 2010;29(2):273–81.
11. Wharton S, Schafer A, Bowtell R. Susceptibility mapping in the human brain using threshold-based k-space division. Magn Reson Med. 2010;63(5):1292–304.
12. Cronin MJ, Wang N, Decker KS, Wei H, Zhu WZ, Liu C. Exploring the origins of echo-time-dependent quantitative susceptibility mapping (QSM) measurements in healthy tissue and cerebral microbleeds. Neuroimage. 2017;149:98–113.
13. Sood S, Urriola J, Reutens D, O'Brien K, Bollmann S, Barth M, et al. Echo time-dependent quantitative susceptibility mapping contains information on tissue properties. Magn Reson Med. 2017;77(5):1946–58.
14. de Rochefort L, Brown R, Prince MR, Wang Y. Quantitative MR susceptibility mapping using piece-wise constant regularized inversion of the magnetic field. Magn Reson Med. 2008;60(4):1003–9.
15. Henkelman M, Kucharczyk W. Optimization of gradient-echo MR for calcium detection. AJNR Am J Neuroradiol. 1994;15(3):465–72.
16. Schofield MA, Zhu Y. Fast phase unwrapping algorithm for interferometric applications. Opt Lett. 2003;28(14):1194–6.

17. Zhou D, Liu T, Spincemaille P, Wang Y. Background field removal by solving the Laplacian boundary value problem. NMR Biomed. 2014;27(3):312–9.
18. Liu J, Liu T, de Rochefort L, Ledoux J, Khalidov I, Chen W, et al. Morphology enabled dipole inversion for quantitative susceptibility mapping using structural consistency between the magnitude image and the susceptibility map. Neuroimage. 2012;59(3):2560–8.
19. Liu T, Xu W, Spincemaille P, Avestimehr AS, Wang Y. Accuracy of the morphology enabled dipole inversion (MEDI) algorithm for quantitative susceptibility mapping in MRI. IEEE Trans Med Imaging. 2012;31(3):816–24.
20. Gilbert G, Savard G, Bard C, Beaudoin G. Quantitative comparison between a multiecho sequence and a single-echo sequence for susceptibility-weighted phase imaging. Magn Reson Imaging. 2012;30(5):722–30.
21. Sun H, Kate M, Gioia LC, Emery DJ, Butcher K, Wilman AH. Quantitative susceptibility mapping using a superposed dipole inversion method: application to intracranial hemorrhage. Magn Reson Med. 2016;76(3):781–91.
22. Li J, Chang S, Liu T, Jiang H, Dong F, Pei M, et al. Phase-corrected bipolar gradients in multi-echo gradient-echo sequences for quantitative susceptibility mapping. MAGMA. 2015;28(4):347–55.
23. Wang Y. Quantitative susceptibility mapping: magnetic resonance imaging of tissue magnetism. Scotts Valley: CreateSpace Independent Publishing Platform; 2013. p. 57–82.
24. Blazejewska AI, Wharton S, Gowland PA, Bowtell R. Understanding the effects of oriented susceptibility inclusions on the phase and magnitude of gradient echo signals. In: Proceedings of 19th Annual Meeting ISMRM, Montréal, 2011; p 4511.
25. Robinson SD, Dymerska B, Bogner W, Barth M, Zaric O, Goluch S, et al. Combining phase images from array coils using a short echo time reference scan (COMPOSER). Magn Reson Med. 2017;77(1):318–27.
26. Shmueli K, de Zwart JA, van Gelderen P, Li TQ, Dodd SJ, Duyn JH. Magnetic susceptibility mapping of brain tissue in vivo using MRI phase data. Magn Reson Med. 2009;62(6):1510–22.
27. Bilgic B, Fan AP, Polimeni JR, Cauley SF, Bianciardi M, Adalsteinsson E, et al. Fast quantitative susceptibility mapping with L1-regularization and automatic parameter selection. Magn Reson Med. 2014;72(5):1444–59.